Ice *vs*. steel: Ballistic impact of woven carbon/epoxy composites. Part II – Numerical modelling

Laurence A. Coles, Anish Roy, Vadim V. Silberschmidt*

Wolfson School of Mechanical, Electrical and Manufacturing Engineering, Loughborough University, Leicestershire LE11 3TU, UK

A B S T R A C T

Part I of this study covered ballistic tests, in which both solid (steel) and fragmenting (ice) spherical projectiles were fired at specimens of carbon-fibre-reinforced polymer (CFRP) composite. The velocity of impacts varied from 70 to 90 m/s for the solid projectiles and from 300 to 500 m/s for the fragmenting projectiles, resulting in three consistent and comparable levels of structural damage for both types of projectiles. The observed dynamic deformation behaviour and resultant damage were examined using a combination of non-invasive analysis techniques. The focus of this Part II is on the development of a mesoscale modelling strategy for CFRP employing a phenomenological continuum-damage approach. The developed model was validated against the data from original ballistic-impact experiments, demonstrating accurate predictions of both deformation behaviour and observed resultant damage of tested specimens for the various experimental loading conditions without modification of the modelling parameters.

Keywords:
Fibre-reinforced composites
Delamination
Impact behaviour
Finite-element analysis
Constitutive modelling

1. Introduction

This work presents the numerical modelling of ballistic impact tests of carbon-fibre-reinforced polymer (CFRP) specimens with two types of projectile – solid (steel) and fragmenting (ice) – presented in Part I of this paper. Here, a mesoscale modelling strategy for CFRPs is proposed based on a phenomenological continuum-damage approach, directly related to the deformation and damage analysis in Part I. In addition to the literature review presented in Part I, the remainder of this introduction focuses solely on numerical modelling of CFRPs.

Numerical methods have been widely employed for the design of components, and over the last decades have been increasingly utilised for the analysis of deformation and damage of composite materials. The finite-element method (FEM) was used to model the respective mechanisms at mesoscale, with homogenisation assumptions applied to capture the microscale damage mechanisms while achieving improved computational efficiency. Though extensive research was conducted on the ballistic impact of composites for a specific type of projectile, a comprehensive study detailing the nature of damage due to the impacts with solid and fragmenting projectiles is lacking. A thorough literature survey revealed one study detailing some aspects of the problem studied here [1]. In recent years effort was made towards understanding the impact process of ice projectiles and its effect on CFRP specimens but to date, there are no direct comparisons to that of rigid (steel) projectile, especially including numerical modelling.

Modelling with a mesoscale approach of a macroscale response of a composite component allows accuracy and computational efficiency thanks to avoiding small element sizes usually employed in simulations of individual composite constituents. So, the

* Corresponding author at: Wolfson School of Mechanical, Electrical and Manufacturing Engineering, Loughborough University, Ashby Road, Leicestershire LE11 3TU, UK.

E-mail addresses: L.A.Coles@lboro.ac.uk (L.A. Coles), A.Roy3@lboro.ac.uk (A. Roy), V.Silberschmidt@lboro.ac.uk (V.V. Silberschmidt).

Nomenclature

$\boldsymbol{C}(d)_{ijkl}$	fourth-order stiffness tensor
de_{ii}	damage evolution parameters in each of the orthogonal directions
de_{ij}	damage evolution parameters in each of the shear directions
di_{ii}	damage initiation parameters in each of the orthogonal directions
E	elastic modulus
E_{33}	stiffness of the CFRP ply in the through-thickness direction
G_c	energy release rate
G_f	damage evolution energy release rate
G_{ij}	shear moduli in each of the shear directions
G_n, G_s, G_t	instantaneous interlaminar fracture energies in the normal and shear directions (mode I, II and III)
G_n^0,G_s^0, G_t^0	interlaminar critical energy values (mode I, II and III)
k_n, k_s, k_t	interlaminar stiffness (mode I, II and III)
K	interface stiffness
l_{cz}	maximum global seed size of the mesh
L_c	characteristic element length
m_e, m_x	material parameters
M	parameter
S_{ij}	shear strengths in each of the shear directions
t	thickness of the CFRP ply
t_n, t_s, t_t	instantaneous interlaminar stress (mode I, II and III)
t_n^0,t_s^0, t_t^0	maximum interlaminar strength (mode I, II and III)
X_{iic}	compressive strengths in each of the orthogonal directions
X_{iit}	tensile strengths in each of the orthogonal directions
X_{ii}^{Dyn}	dynamic strength in each of the orthogonal directions
α	parameter
β	parameter in the mixed-mode power-law criterion
γ_{ij}	second-order shear strain tensor
γ_{ij}^{e}	elastic component of shear strain
γ_{ij}^{f}	shear strain at complete damage evolution
γ_{ij}^{in}	inelastic component of shear strain
$\gamma_{ij,0}^{in}$	inelastic shear strain at damage initiation
ε_{ii}^{0}	equivalent strain at damage initiation
ε_{ii}^{f}	strain at complete damage evolution
$\boldsymbol{\varepsilon}_{kl}$	second-order strain tensor
ν_{ij}	Poisson's ratio in each of the shear directions
$\boldsymbol{\sigma}_{ij}$	second-order stress tensor
τ^0	ultimate interface strength
τ_{ij}	second order shear stress tensor

laminate structure of CFRPs can be formed by stacking the anisotropic homogeneous plies at different angles, depending on the fibre orientation and stacking sequence. The meshing could then be performed with solid elements, with full continuum-based 3D elasticity models for single plies, with cohesive-zone elements or surfaces with a traction-separation law employed typically between the neighbouring plies to model the delamination mechanisms (including initiation and propagation). This allows for the intra-ply and inter-ply damage mechanisms to be modelled separately at the macro scale, enabling the complex analysis of the interaction between these mechanisms. This was demonstrated to be an excellent method for modelling larger components subjected to complex loading conditions including impact regimes while providing good accuracy in predicting the failure behaviour when compared with experimental validation (see e.g. [2–7]). For this mesoscale modelling approach, it is very important to include all six degrees of freedom in a solid-element formulation based on the 3D continuum elasticity theory. Only in this case can delamination and interlaminar shear behaviour be captured along with the adequate assessment of through-thickness normal stress components, allowing a more accurate assessment of the failure of the composite.

A popular approach to predict the initiation of various failure mechanisms in a ply of a fibre-reinforced composite utilises the tracking and accumulation of damage until the ply reaches the state of ultimate failure. The simplest and most commonly used way of doing this is via continuum damage mechanics (CDM), first proposed by Kachanov [8]. This approach is used to predict the stiffness degradation and damage evolution over time as damage accumulates. This approach introduces a damage variable into the constitutive model describing the initiation and progression of damage and can consider multiple separate damage mechanisms. This approach became popular in the analysis of composites following the work by Talreja [9,10], and describes the damage as the appearance of cracks, diminishing the associated area supporting the applied load. This is equivalent to defining the effective strain or stress associated with the damage. Early variants of this approach, such as the Matzenmiller-Lubliner-Taylor (MLT) model [11], were developed to include strain softening and account for damage in warp, weft and shear directions. These schemes were then developed further to incorporate specific features related to a continuum-based description of woven composites [12].

Complex fragmentation behaviour of ice projectiles presupposes the development of methods suitable for failure analysis of the projectile. Pernas-Sánchez et al. [13] utilised the Drucker–Prager criterion, accounting for asymmetric tensile/compressive plastic behaviour. Additionally, a failure criterion based on tensile-pressure cut-off was used to describe the process of ice fragmentation. Using this scheme, three numerical approaches were examined to model to the large-deformation behaviour, producing a complex loading condition: Lagrangian meshing, adaptive Lagrangian-Eulerian formulation and smooth particle hydrodynamics (SPH). The study concluded that all the used methods adequately reproduced the ice behaviour in terms of forces induced in the impact. Another approach for modelling the behaviour of ice was presented by Tippman et al. [14]. In their study, a model based on a strain-rate-dependent compressive strength was employed also with a failure criterion based on tensile pressure cut-off to describe the ice fragmentation. Results from their study showed a good correlation with experimental data for the effect of the kinetic energy of projectiles on a peak impact force.

This part has the following structure: after a brief overview in Section 2 of the specimens and the experimental setup presented in Part I, the development of a mesoscale modelling strategy for CFRPs is discussed in Section 3. Next, results of the numerical

simulations for two types of the studied projectiles are compared to the experimental data from Part I in Section 4, followed by concluding remarks in Section 5.

2. Description of experiments

For the convenience of the reader, a brief overview of the composite specimens, projectiles and the experimental test regime is provided below in order to give sufficient information for the numerical modelling; full details can be found in Part I.

2.1. Material specification

The CFRP specimens used for the case studies measured 195 × 195 mm^2 and were fabricated from 10 plies of carbon-fibre fabric, pre-impregnated with toughened epoxy IMP530R. The 2 × 2 twill weave plies were formed into a laminate consisting of 2 surface plies (T300 3 K) with an approximate thickness of 0.31 mm and 8 central plies (T300 12 K) with an approximate thickness of 0.62 mm, resulting in a total panel thickness of 5.6 mm. A used 0°/90° layup configuration resulted in nominally orthotropic behaviour.

2.2. Projectiles and test methodologies

All the solid (steel) projectiles had a diameter of 23.8 mm with a weight of 54.7 g, and the ice projectiles (hail-stone imitation) had a diameter 25 mm with a weight of 7.5 g at a temperature of −20 °C.

The CFRP specimens were installed and aligned with the barrel, using a cantilever clamping regime, with all specimens subjected to an orthogonal impact as shown in Fig. 1. The projectile was accelerated to the required speed in the barrel using compressed air, and the impact process was captured with two high-speed cameras (Photron Fastcam SA5). The choice of impact velocities resulted in three levels of ballistic damage induced: minor, medium and major (with full/partial penetration). Solid (steel) projectiles were used at 58 m/s, 78 m/s, 90 m/s while the respective velocities for the ice projectiles were 300 m/s, 400 m/s, 480 m/s.

3. Finite-element modelling of CFRPs

3.1. Material modelling

A mesoscale model for deformation of CFRPs was developed with the use of a phenomenological CDM approach. A resultant user-

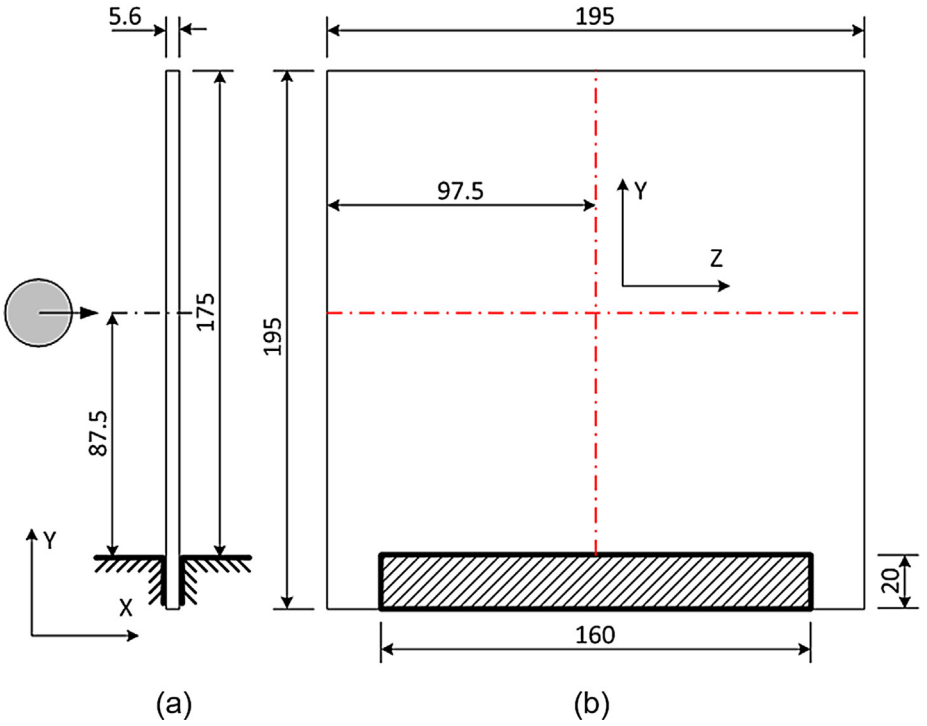

Fig. 1. CFRP specimens in experimental setup with dimensions (in mm), impact location and deformation analysis locations (red lines): (a) side view; (b) front view. (For interpretation of the references to colour in this figure legend, the reader is referred to the web version of this article.)

defined material subroutine (VUMAT) was implemented into the ABAQUS Explicit (6.14-4) solver. The constitutive description combines the advantages of damage model proposed by Hashin [15] and Puck [16], which were suitably modified in order to analyse a woven laminate along with the through-thickness stress response [6]. Damage evolution until failure was modelled using the concept of equivalent displacement, with mesh-sensitivity mitigated by incorporating a characteristic length of a finite-element in the formulation. Material parameters for all the equations are discussed in Section 3.8.2.

3.2. Elasticity and stiffness degradation

Woven plies of CFRP were assumed orthotropic. A damage tensor was used to calculate the effective stress as a result of stiffness degradation with the CDM-based approach. The elastic stress tensor is evaluated from

$$\boldsymbol{\sigma}_{ij} = \boldsymbol{C}(d)_{ijkl}\boldsymbol{\varepsilon}_{kl}, \tag{1}$$

where σ and ε are the second-order stress and strain tensors, respectively, $\mathbf{C}(d)$ is the fourth-order stiffness tensor depending on damage d.

3.3. Damage initiation

To evaluate fibre failure modes within the composite plies, a modified version of Hashin's failure criteria were incorporated into the model using the following equations:

Tensile fibre failure in the fill 11 direction

$$\left(\frac{\sigma_{11}}{X_{11t}^{dyn}}\right)^2 + \left(\frac{\sigma_{12}}{S_{12}}\right)^2 + \left(\frac{\sigma_{13}}{S_{13}}\right)^2 \geq 1 \tag{2}$$

Tensile fibre failure in the wrap 22 direction

$$\left(\frac{\sigma_{22}}{X_{22t}^{dyn}}\right)^2 + \left(\frac{\sigma_{12}}{S_{12}}\right)^2 + \left(\frac{\sigma_{23}}{S_{23}}\right)^2 \geq 1 \tag{3}$$

Compressive fibre failure in the fill 11 direction

$$\left(\frac{\sigma_{11}}{X_{11c}^{dyn}}\right)^2 + \left(\frac{\sigma_{12}}{S_{12}}\right)^2 + \left(\frac{\sigma_{13}}{S_{13}}\right)^2 \geq 1 \tag{4}$$

Compressive fibre failure in the wrap 22 direction

$$\left(\frac{\sigma_{22}}{X_{22c}^{dyn}}\right)^2 + \left(\frac{\sigma_{12}}{S_{12}}\right)^2 + \left(\frac{\sigma_{23}}{S_{23}}\right)^2 \geq 1 \tag{5}$$

Matrix-failure modes within the plies are then evaluated with a modified version of the Puck's failure criterion, for the woven composite plies and matrix failure relating to any of directions within the 3D continuum elements [16]. This is described as

$$\left(\frac{\sigma_{11}^2}{2X_{11}^{dyn}}\right) + \left(\frac{\sigma_{22}^2}{2X_{22}^{dyn}}\right) + \left(\frac{\sigma_{12}}{S_{12}}\right)^2 + \left(\frac{\sigma_{13}}{S_{13}}\right)^2 + \left(\frac{\sigma_{23}}{S_{23}}\right)^2 + \left(\frac{\sigma_{33}^2}{X_{33t}^{dyn}X_{33c}^{dyn}}\right) + \sigma_{33}\left(\frac{1}{X_{33t}^{dyn}} + \frac{1}{X_{33c}^{dyn}}\right) \geq 1,$$

$$\text{Tensile failure} \rightarrow \sigma_{33} > 0,$$

$$\text{Compressive failure} \rightarrow \sigma_{33} < 0.$$

3.4. Shear response

A shear response of a composite is often dominated by non-linear behaviour of the matrix while undergoing stiffness degradation. Therefore, a non-linear semi-empirical shear model was included in the constitutive description to capture this shear behaviour [17,18]. The shear stress was evaluated from

$$\tau_{ij} = S_{ij}\left[1 - \exp\left(-\frac{G_{ij}^0\gamma_{ij}}{S_{ij}}\right)\right], \tag{6}$$

where S_{ij} is the ultimate shear strength, G_{ij}^0 is the shear modulus and γ_{ij} is the instantaneous shear strain. Damage initiation (di_{ij}) in each of the shear directions was calculated from

$$di_{ij} = \frac{\sigma_{ij}}{S_{ij}}(i \neq j). \tag{7}$$

3.5. Damage evolution

Damage evolution was assumed to accumulate along a bilinear path tensile and compressive failure modes in local coordinates. This approach to continuum stiffness degradation was developed for the 2 × 2 twill woven CFRP, and calculated using the following equation:

$$de_{ii} = \frac{\varepsilon_{ii}^{f}(\varepsilon_{ii} - \varepsilon_{ii}^{0})}{\varepsilon_{ii}(\varepsilon_{ii}^{f} - \varepsilon_{ii}^{0})} \tag{8}$$

where ε_{ii} is the current equivalent strain, ε_{ii}^{0} is the equivalent strain, at which damage initiation $di_{ij} = 0$, obtained from Eq. (7), ε_{ii}^{f} is the strain, at which damage evolution is complete $di_{ij} = 1$ (fully damaged). These equations were then used to calculate damage evolution for both tensile and compressive failure modes in local coordinates.

For shear directions, in which non-linear behaviour was included, the instantaneous shear strain γ_{ij} was split in elastic γ_{ij}^{e} and inelastic γ_{ij}^{in} components using the following relation:

$$\gamma_{ij}^{in} = \gamma_{ij} - \gamma_{ij}^{e} = \gamma_{ij} - \frac{\tau_{ij}}{G_{ij}^{0}}(i \neq j) \tag{9}$$

where τ_{ij} and G_{ij}^{0} are the non-linear shear stress and shear modulus in each shear direction. Shear damage evolution was assessed using [7]

$$de_{ij} = \frac{\gamma_{ij}^{f}[2(\gamma_{ij} - \gamma_{ij,0}^{in}) - \gamma_{ij}^{f}]}{(\gamma_{ij}^{f} + \gamma_{ij,0}^{in} - \gamma_{ij})(\gamma_{ij} - \gamma_{ij,0}^{in})} \tag{10}$$

Here, $\gamma_{ij,0}^{in}$ is the inelastic shear strain at damage initiation and γ_{ij}^{f} is the shear failure strain.

The failure displacements were calculated from the defined failure energies and derived from the following expression in the normal and shear directions:

$$\delta_{ii}^{f} = \frac{2G_{f}}{X_{ii}},\ \delta_{ij}^{f} = \frac{2G_{f}}{S_{ij}}, \tag{11}$$

where G_{f} is the failure energy in the given direction, X_{ii} is the normal failure stress and S_{ij} is the shear failure stress.

A characteristic length for mesh-dependency was incorporated into this equation by converting the displacement to strain in the given direction using the parameter L_{c}, such that $\delta_{ii}^{f} = L_{c}\varepsilon_{ii}^{f}$ for the normal direction, making the final form for both normal and shear directions as follows [7]:

$$\varepsilon_{ii}^{f} = \frac{2G_{f}}{X_{ii}L_{c}},\ \gamma_{ij}^{f} = \frac{2G_{f}}{S_{ij}L_{c}} \tag{12}$$

Element deletion was employed to remove elements in the FE mesh once damage associated with fibre failure reached a value of 1 in

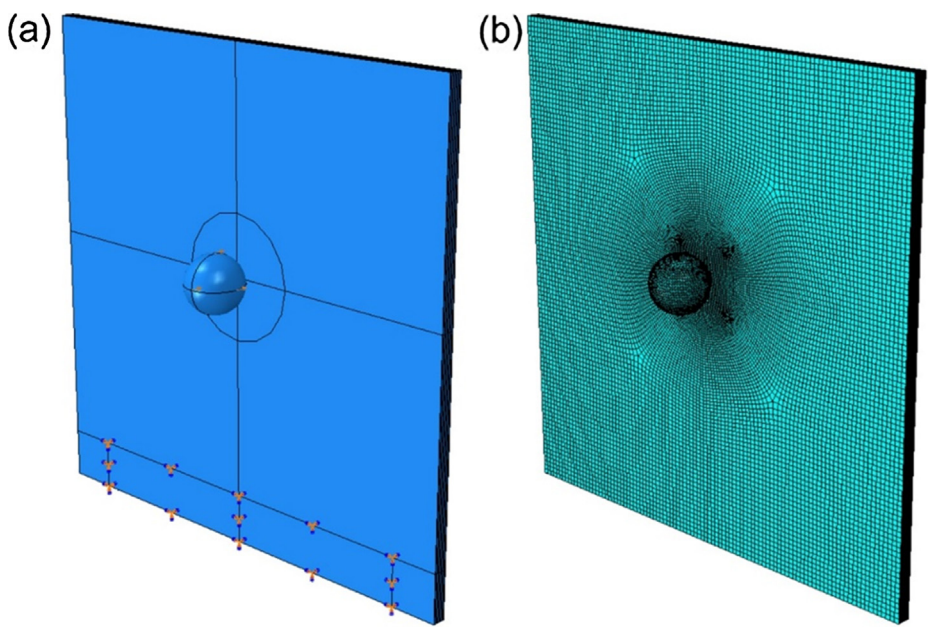

Fig. 2. Ballistic impact model: (a) geometry and boundary conditions; (b) mesh.

Table 1
Material parameters of steel.

Parameter	Value	Unit
Elastic modulus: E	210.0	(GPa)
Poisson's ratio: ν	0.3	–
Density: ρ	7600	(kg/m^3)

Table 2
Material parameters of ice [14].

Parameter	Value	Unit
Elastic modulus: E	9.38	(GPa)
Poisson's ratio: ν	0.33	–
Density: ρ	900	(kg/m^3)
Tensile failure pressure	0.517	(MPa)
Compressive yield strength	5.2	(MPa)

Strain rate (s^{-1})	Compressive yield ratio
0	1
0.1	1.01
0.5	1.50
1	1.71
5	2.20
10	2.42
50	2.91
100	3.13
500	3.62
1000	3.84
5000	4.33
10,000	4.55
50,000	5.04
100,000	5.25
500,000	5.75
1,000,000	5.96

either 11 or 22 direction (in practice, a value of 0.999 was chosen).

3.6. Strain-rate sensitivity

A strain rate is known to affect the mechanical response of laminated composites [19,20], with the exception of fracture energy (ultimate failure strain) [21]. So, the elastic modulus and strength were defined as [20]

$$E(\dot{\varepsilon}) = E(\dot{\varepsilon_0})\left[m_e \log\left(\frac{\dot{\varepsilon}}{\dot{\varepsilon_0}}\right) + 1\right] \tag{13}$$

$$X(\dot{\varepsilon}) = X(\dot{\varepsilon_0})\left[m_x \log\left(\frac{\dot{\varepsilon}}{\dot{\varepsilon_0}}\right) + 1\right] \tag{14}$$

where $E(\dot{\varepsilon})$ is the updated elastic modulus at the given strain rate, $E(\dot{\varepsilon_0})$ is the elastic modulus at the reference strain rate, $\dot{\varepsilon}$ is the current strain rate and m_e is a material parameter that is calibrated with experimentally obtained data. Next, $X(\dot{\varepsilon})$ is the updated strength at the current strain rate, $X(\dot{\varepsilon_0})$ is the original strength at the quasi-static strain rate and m_x is a scaling parameter that requires calibration.

3.7. Delamination modelling

Delamination of the individual CFRP plies was modelled with the use of cohesive-zone surfaces (CZS) available in Abaqus Explicit by employing a bi-linear traction-separation law, with the degradation of the inter-ply region propagating under the combined influence of normal and shear stresses via a quadratic nominal stress criterion,

$$\left[\frac{t_n}{t_n^0}\right]^2 + \left[\frac{t_s}{t_s^0}\right]^2 + \left[\frac{t_t}{t_t^0}\right]^2 = 1 \tag{15}$$

Here, t_n, t_t and t_s are the instantaneous components of normal and shear tractions at the surface, while t_n^0, t_t^0 and t_s^0 are the maximum

Table 3
Extrapolated CFRP model parameters – elastic [20,24–31].

Ref	$E_{11t\,\&\,22t}^{Quasi}$ (GPa)	E_{33t}^{Quasi} (GPa)	$E_{11c\,\&\,22c}^{Quasi}$		E_{33c}^{Quasi}		$E_{11t\,\&\,22t}^{Dyn}$		E_{33t}^{Dyn}		$E_{11c\,\&\,22c}^{Dyn}$		E_{33c}^{Dyn}		G_{12}^{Quasi} (GPa)	$G_{23\,\&\,13}^{Quasi}$ (GPa)	ν_{12}	$\nu_{23\,\&\,13}$
			(GPa)	$\frac{E_{11c\,\&\,22c}^{Quasi}}{E_{11t\,\&\,22t}^{Quasi}}$	(GPa)	$\frac{E_{33c}^{Quasi}}{E_{33t}^{Quasi}}$	(GPa)	$\frac{E_{11t\,\&\,22t}^{Dyn}}{E_{11t\,\&\,22t}^{Quasi}}$	(GPa)	$\frac{E_{33t}^{Dyn}}{E_{33t}^{Quasi}}$	(GPa)	$\frac{E_{11c\,\&\,22c}^{Dyn}}{E_{11c\,\&\,22c}^{Quasi}}$	(GPa)	$\frac{E_{33c}^{Dyn}}{E_{33c}^{Quasi}}$			–	–
Studied CFRP	51.0	8.0																
[31]	59.0	8.0													3.8	3.0	0.050	0.300
[30]	59.5														3.4		0.100	
[29]	60.0														4.9		0.060	
[28]	51.8		48.2	0.931											2.9		0.042	
[27]	69.1		58.7	0.849											4.4		0.050	
[26]	68.3						69.9	1.024							4.8		0.055	
[25]		10.5							10.5	1.000								
[24]					5.1								5.6	1.098				
[20]					11.2								14.5	1.295				
Averages	61.28	9.25	53.45	0.890	8.15	1.00	69.90	1.024	10.50	1.000	–	–	10.05	1.196	4.03	3.00	0.060	0.300
CFRP model parameters	51.0	8.0		45.4		8.0		52.2		8.0		46.5		9.6	4.032	3.000	0.060	0.300

Table 4
Extrapolated CFRP model parameters – strength [20,24–31].

Ref	$F_{11t\,\&\,22t}^{Quasi}$	F_{33t}^{Quasi}	$F_{11c\,\&\,22c}^{Quasi}$		F_{33c}^{Quasi}		$F_{11t\,\&\,22t}^{Dyn}$		F_{33t}^{Dyn}		$F_{11c\,\&\,22c}^{Dyn}$		F_{33c}^{Dyn}		S_{12}^{Quasi}	$S_{23\,\&\,13}^{Quasi}$	S_{12}^{Dyn}	$S_{23\,\&\,13}^{Dyn}$
	(MPa)	(MPa)	(MPa)	$\frac{F_{11c\,\&\,22c}^{Quasi}}{F_{11t\,\&\,22t}^{Quasi}}$	(MPa)	$\frac{F_{33c}^{Quasi}}{F_{33t}^{Quasi}}$	(MPa)	$\frac{F_{11t\,\&\,22t}^{Dyn}}{F_{11t\,\&\,22t}^{Quasi}}$	(MPa)	$\frac{F_{33t}^{Dyn}}{F_{33t}^{Quasi}}$	(MPa)	$\frac{F_{11c\,\&\,22c}^{Dyn}}{F_{11c\,\&\,22c}^{Quasi}}$	(MPa)	$\frac{F_{33c}^{Dyn}}{F_{33c}^{Quasi}}$	(MPa)	(MPa)	(MPa)	(MPa)
Studied CFRP	520.0	73.0																
[31]	859.0		673.0	0.783											120.0			
[30]	597.0														94.0			
[29]	670.0						748.0	1.116							87.0		164.0	
[28]	562.0		602.6	1.071											84.1			
[27]	592.0		497.0	0.840											83.0			
[26]	545.0		507.0	0.930			637.0	1.169			914.0	1.803			128.0		225.0	
[25]		79.0							124.0	1.570								
[24]					778.0								630.0	0.810				
[20]		65.0			285.0	4.385			90.0	1.385			390.0	1.368				
Averages	637.6	72.0	569.9	0.91	531.5	4.38	692.5	1.14	107.0	1.48	914.0	1.80	510.0	1.09	100.0		194.5	
CFRP Model parameters	520.0	73.0		471.2		320.1		594.2		107.8		849.4		348.6	100.0	100.0	194.5	194.5

Table 5
Energy of damage evolution in CFRP [23].

Parameter	Value	Unit
G_{ft}	75,000	(J/m^2)
G_{fc}	25,000	(J/m^2)
G_{mt}	2500	(J/m^2)
G_{mc}	2500	(J/m^2)
G_{sh}	2250	(J/m^2)

Table 6
Delamination material parameters for woven CFRP [22,23].

Parameter	Value	Unit
k_n^o	7.45E5	(GPa)
k_t^o	2.87E5	(GPa)
k_s^o	2.87E5	(GPa)
t_n^o	73.0	(MPa)
t_t^o	100.0	(MPa)
t_s^o	100.0	(MPa)
G_n^o	600	(J/m^2)
G_t^o	5500	(J/m^2)
G_s^o	5500	(J/m^2)

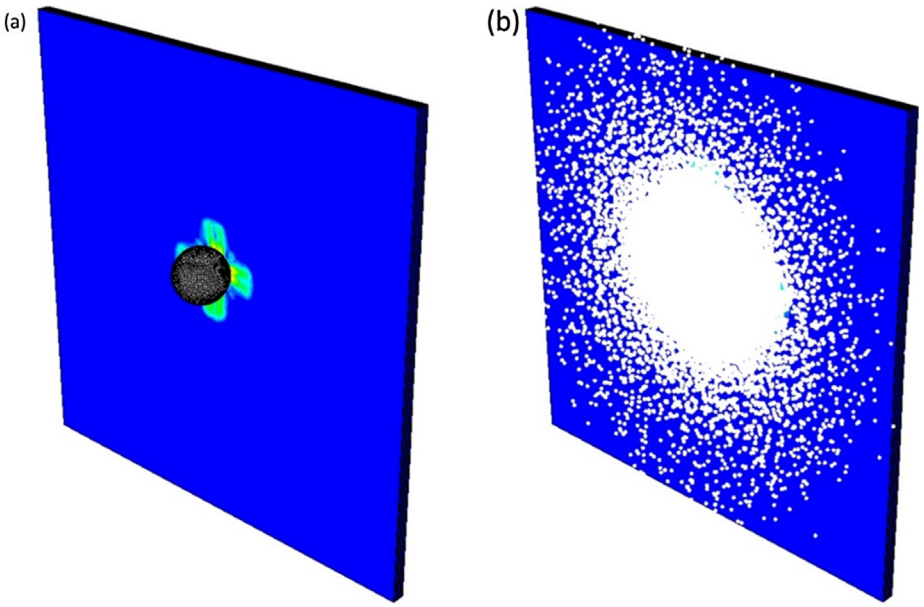

Fig. 3. Results of ballistic impact models at 0.1 ms: (a) steel projectile at 91.5 m/s; (b) ice at 480.0 m/s projectile.

values of the associated stress in each direction. Once this criterion was met, delamination of ply started with stiffness degradation that followed a mixed-mode power-law criterion,

$$\left[\frac{G_n}{G_n^0}\right]^\beta + \left[\frac{G_s}{G_s^0}\right]^\beta + \left[\frac{G_t}{G_t^0}\right]^\beta = 1 \tag{16}$$

Here, G_n, G_t and G_s are the instantaneous fracture energies in both the normal and shear directions, and G_n^0, G_t^0 and G_s^0 are the critical energy values, associated with each direction.

The elastic stiffness was estimated with the empirical formula

$$K = \frac{\alpha E_{33}}{t} \tag{17}$$

where K is the interface stiffness, E_{33} is the stiffness of the CFRP ply in the through-thickness direction, t is the thickness of the

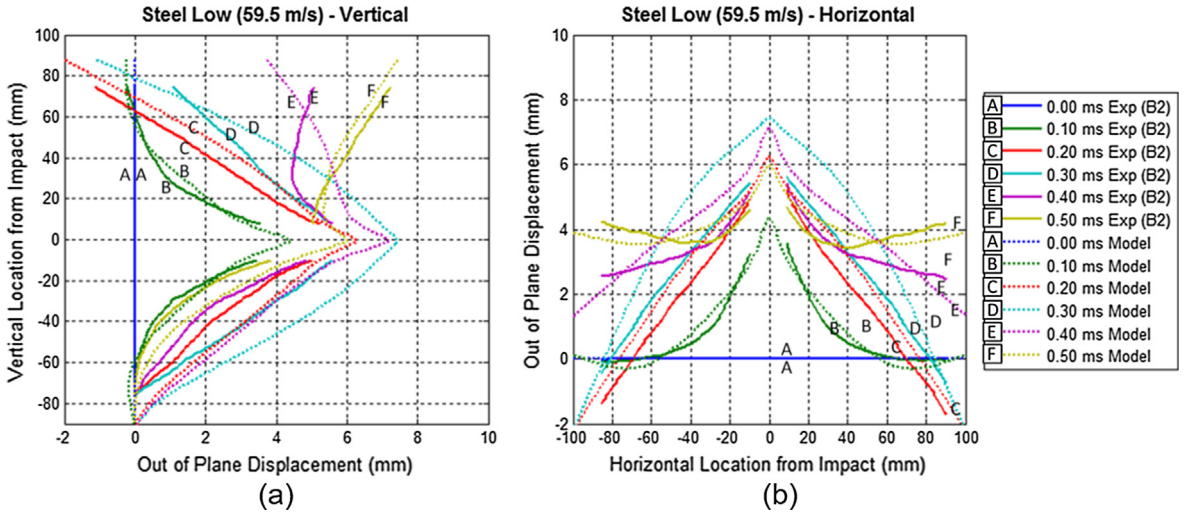

Fig. 4. Out-of-plane displacement of central vertical (a) and horizontal (b) lines (see Fig. 1): experiment *vs.* FE model (steel impact at 59.5 m/s; minor damage).

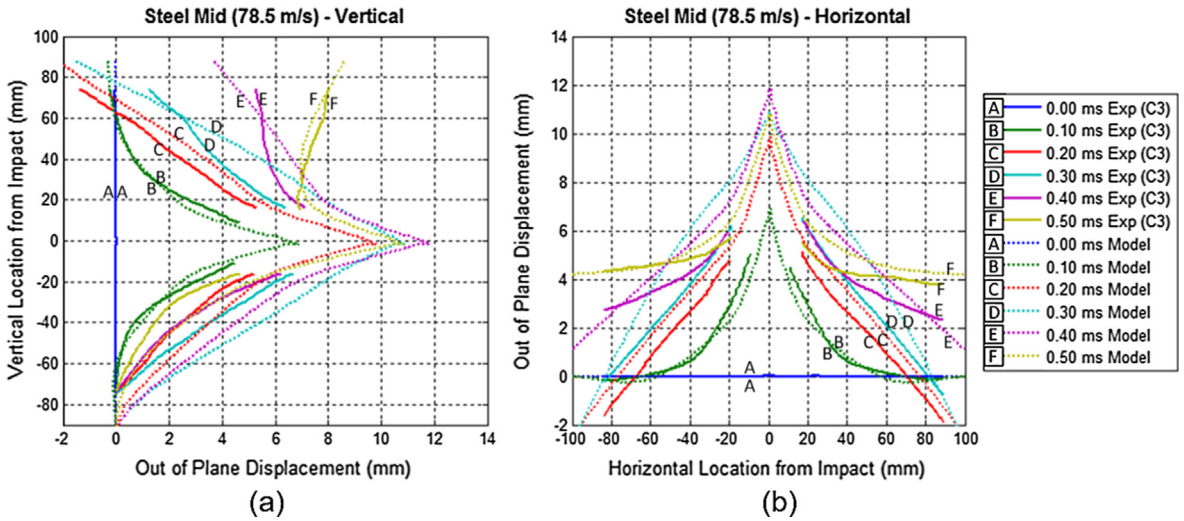

Fig. 5. Out-of-plane displacement of central vertical (a) and horizontal (b) lines (see Fig. 1): experiment *vs.* FE model (steel impact at 78.5 m/s; medium damage).

adjacent CFRP ply, and α=55 is a parameter [22].

3.8. FE model of ballistic setup

3.8.1. Geometry and boundary conditions

The CFRP specimen was modelled using the constitutive phenomenological intra-ply VUMAT model with its parameters defined in Section 3.8.2. The specimen geometry and boundary condition are shown in Fig. 2. The specimen was discretized using 441392 eight-node, isoparametric, hexahedral elements (C3D8R) with 2 elements through the thickness of the surface plies and 3 elements through the thickness of the bulk plies. The mesh was further refined at the location of impact (shown by a circle with a diameter double that of the projectile in Fig. 2) to improve numerical accuracy. A mesh-sensitivity analysis was carried out to ensure that the chosen mesh was appropriate. All results below were obtained with a converged FE model. In it, a minimum element size of 0.5 mm was employed for the centre of the specimen, where maximum damage was expected, while the mesh size at the extremities was ~2 mm.

The rigid projectile was modelled as a linear-elastic solid, using the parameters defined in Table 1. The fragmenting ice projectile was modelled using an SPH failure approach with a model based on strain-rate-dependent compressive strength, with a tensile pressure cut-off failure criteria [14]; the parameters for this model are in Table 2. The projectiles were prescribed a predefined velocity as used in the experiment (see Part I). A schematic of the numerical model including its meshed is shown in Fig. 2.

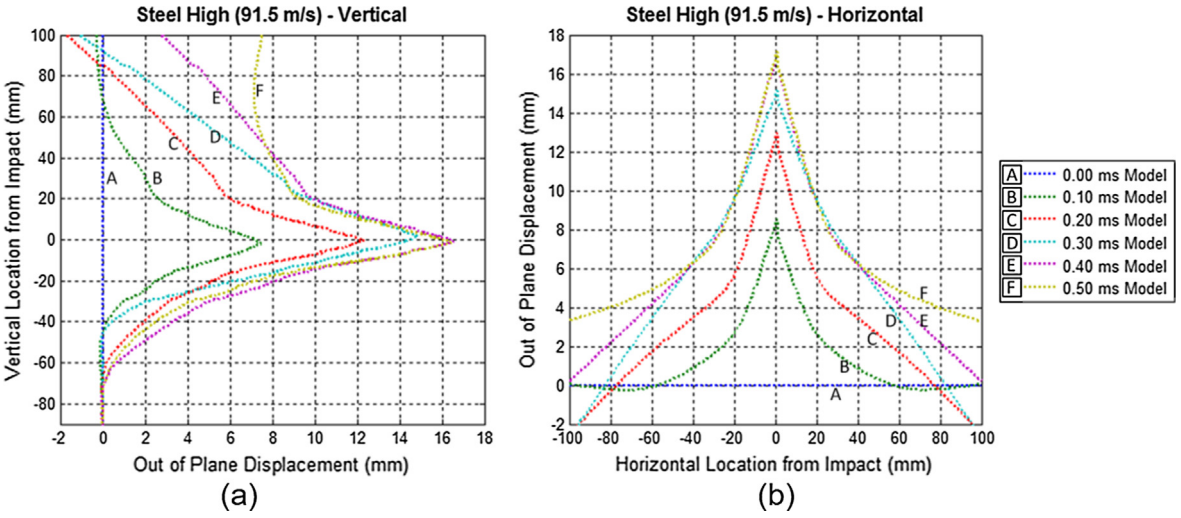

Fig. 6. Out-of-plane displacement of central vertical (a) and horizontal (b) lines (see Fig. 1): experiment *vs*. FE model (steel impact at 91.5 m/s; major damage).

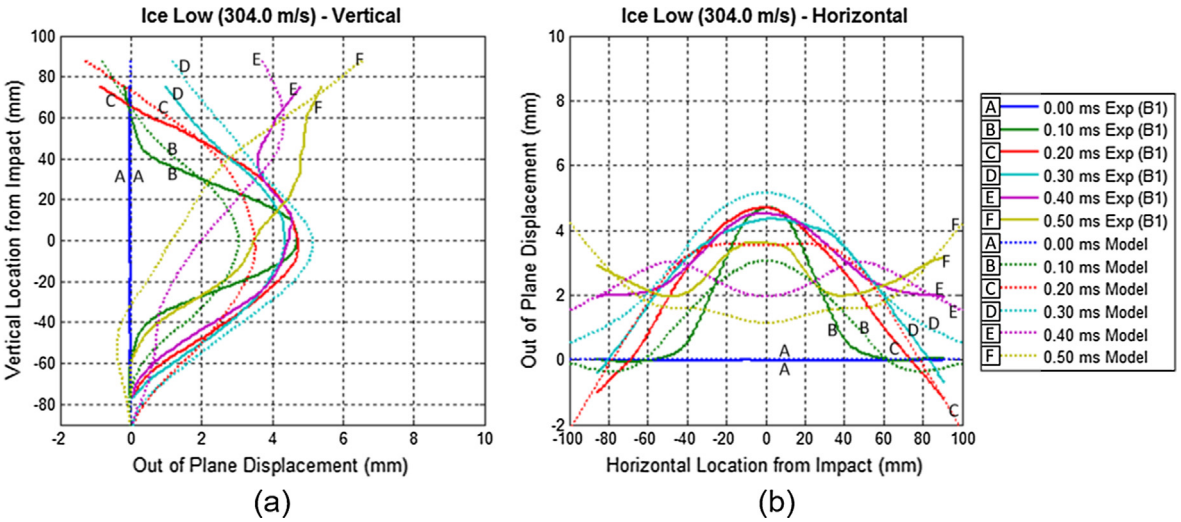

Fig. 7. Out-of-plane displacement of central vertical (a) and horizontal (b) lines (see Fig. 1): experiment *vs*. FE model (ice impact at 304.0 m/s; minor damage).

Cohesive zone surfaces (CZSs) were defined to model delamination. The maximum global seed size of the mesh was determined from

$$l_{cz} = ME\frac{G_c}{(\tau^0)^2} \tag{18}$$

where M is a parameter, E is the elastic modulus of the material, G_c is the energy release rate in the given direction and τ^0 is the ultimate interface strength in the given direction. By using this relation and applying 5 elements across the distance, an approximate element size needed to capture delamination accurately can be obtained [22]. For the suggested model, the maximum adjacent element size was ~2 mm.

3.8.2. Material properties

Based on an extensive literature search, material properties were determined for a similar CFRP with a density of 1480 kg/m^3 and volume fraction using an approach defined in [7]. Parameters used to describe intra-ply behaviour are listed in Tables 3 and 4.

In the case of the dynamic compressive elastic modulus, due to a lack of data, the same dynamic-to-static ratio of tensile behaviour was implemented for compressive one. Only limited data were available for through-thickness behaviour of this 2 × 2 twill woven CFRP; as a result, behaviour of a cross-ply laminate was used to obtain the necessary parameters. The strain-rate-sensitivity relationship for each set of parameters was modelled using the approach proposed in Section 3.6. As there was only limited information

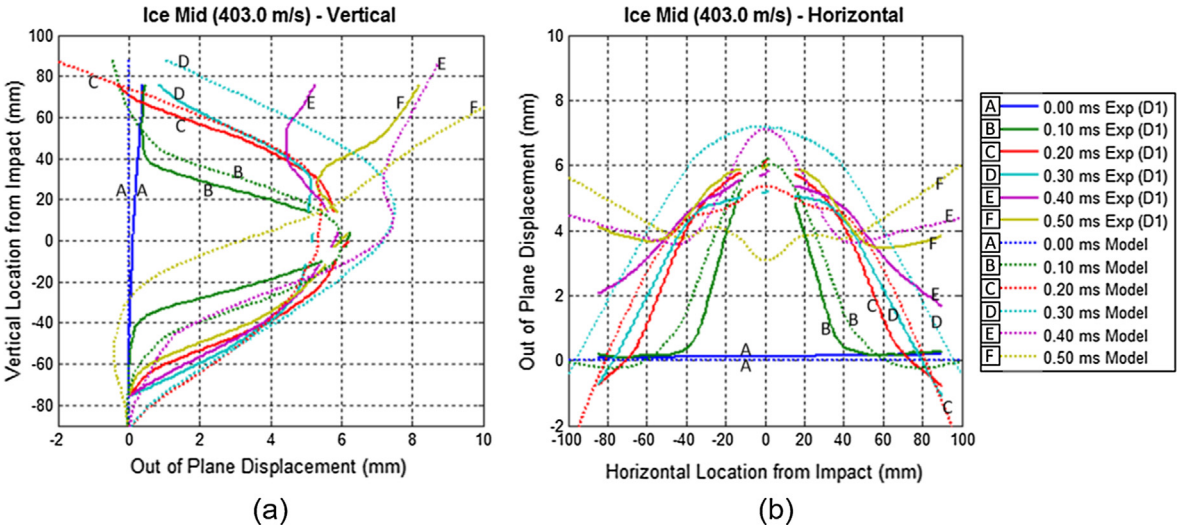

Fig. 8. Out-of-plane displacement of central vertical (a) and horizontal (b) lines (see Fig. 1): experiment *vs*. FE model (ice impact at 403.0 m/s; medium damage).

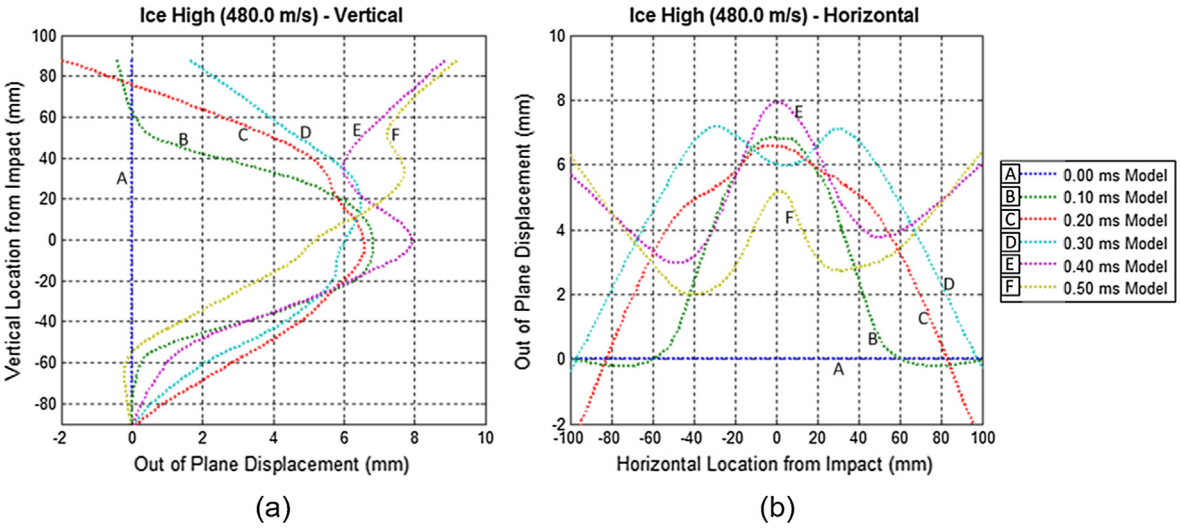

Fig. 9. Out-of-plane displacement of central vertical (a) and horizontal (b) lines (see Fig. 1): experiment *vs*. FE model (ice impact at 480.0 m/s; major damage).

for the strain-rate sensitivity for each of the shear modulus in 3 directions, a strain-rate coefficient $m_e = 0.045$ was assumed [20]. Levels of energy of damage evolution for each considered failure mode are presented in Table 5 [23].

To model delamination using CZSs, the parameters presented in Table 6 were used to describe this inter-ply behaviour [23].

4. Results and discussion

4.1. Deformation analysis

The finite-element models were first validated using the obtained experimental results of deformation analysis. The impacts with two types of studied projectiles at t = 0.1 ms for the major damage state (see Part I) are shown in Fig. 3.

The calculated deformation behaviour of each loading regime with the rigid steel projectile is shown in Figs. 4–6 in comparison to the experiment for the first 0.5 ms of impacts. As can be seen for the low and medium loading velocities (59.5 and 78.5 m/s, respectively), where the DIC data was available, the model result shows a reasonable match with the experimental data for both out-of-plane displacement and the specimen's bending during loading.

Due to the full penetration of the projectile at 91.5 m/s, DIC of the back face of the plate was not possible. So, Fig. 6 presents only computational prediction for deformation of the CFRP specimen in this impact.

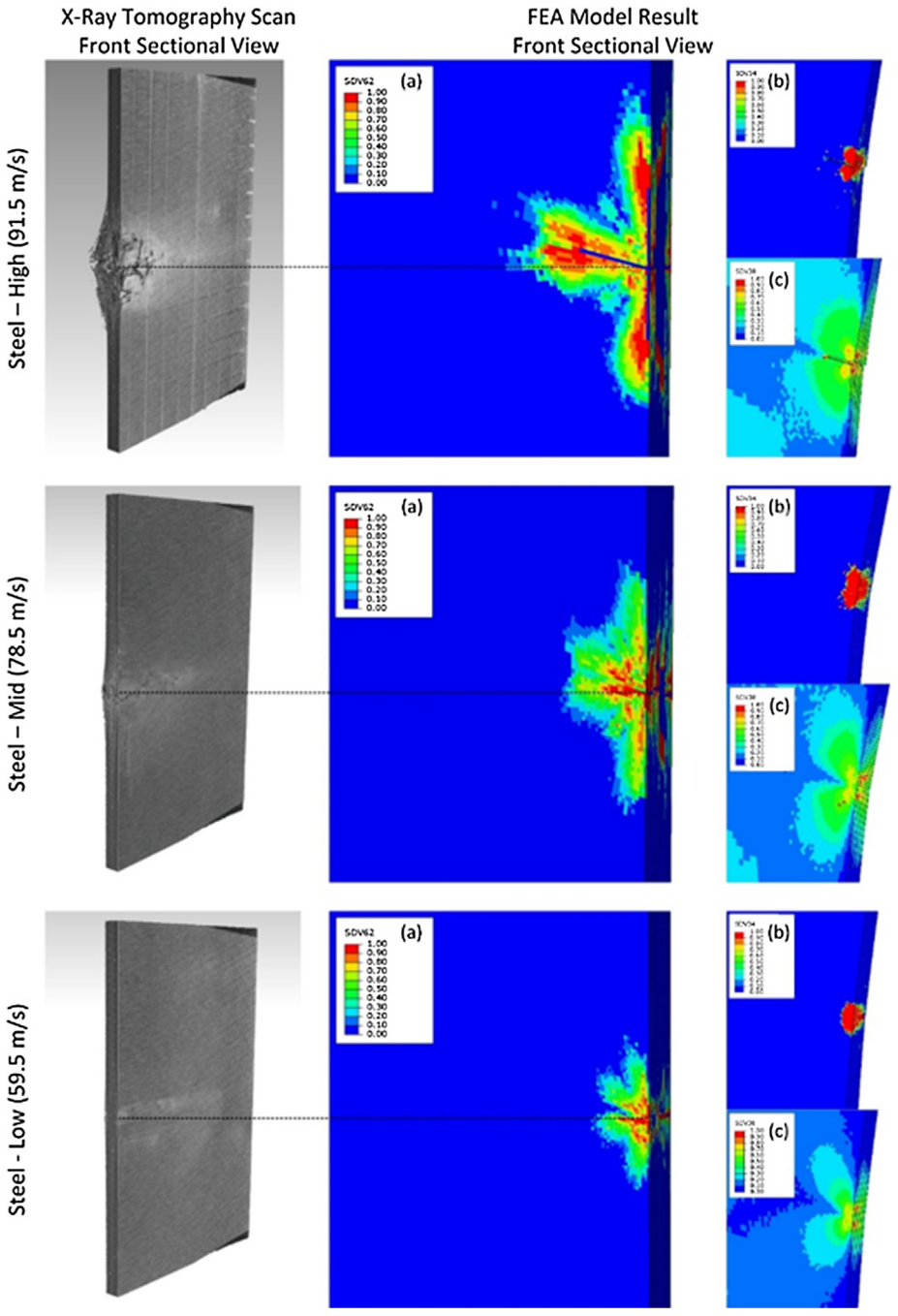

Fig. 10. Ballistic damage in steel-projectile impacts with different velocities: (a) fibre damage; (b) matrix damage; (c) shear damage.

Next, the impact with fragmenting ice projectiles was analysed; deflections from first stages of the slowest impact (304.0 m/s) are compared in Fig. 7. Though a general trend of the deflections matched, there were significant differences in the magnitudes: the experiment demonstrated a higher initial indentation-based deflection. In contrast, deflections caused by the ice impact with the medium velocity (403.0 ms; Fig. 8), exhibited a good correlation between the experimental data and the model. As before, only numerical results are presented for the highest velocity impact (Fig. 9), since experimental data were not recorded due to excessive damage incurred in the specimen.

The general discrepancy between the obtained computational results and the experimental data for the ice-projectile impact is mostly due to a complex nature of the projectile fragmentation, affecting the transient resultant loading condition imposed on the composite specimen. This led to a reduced prediction of the indentation depth in numerical simulations. Still, the maximum out-of-plane displacement showed a reasonable agreement between the numerical and experimental results, with the correct transition of

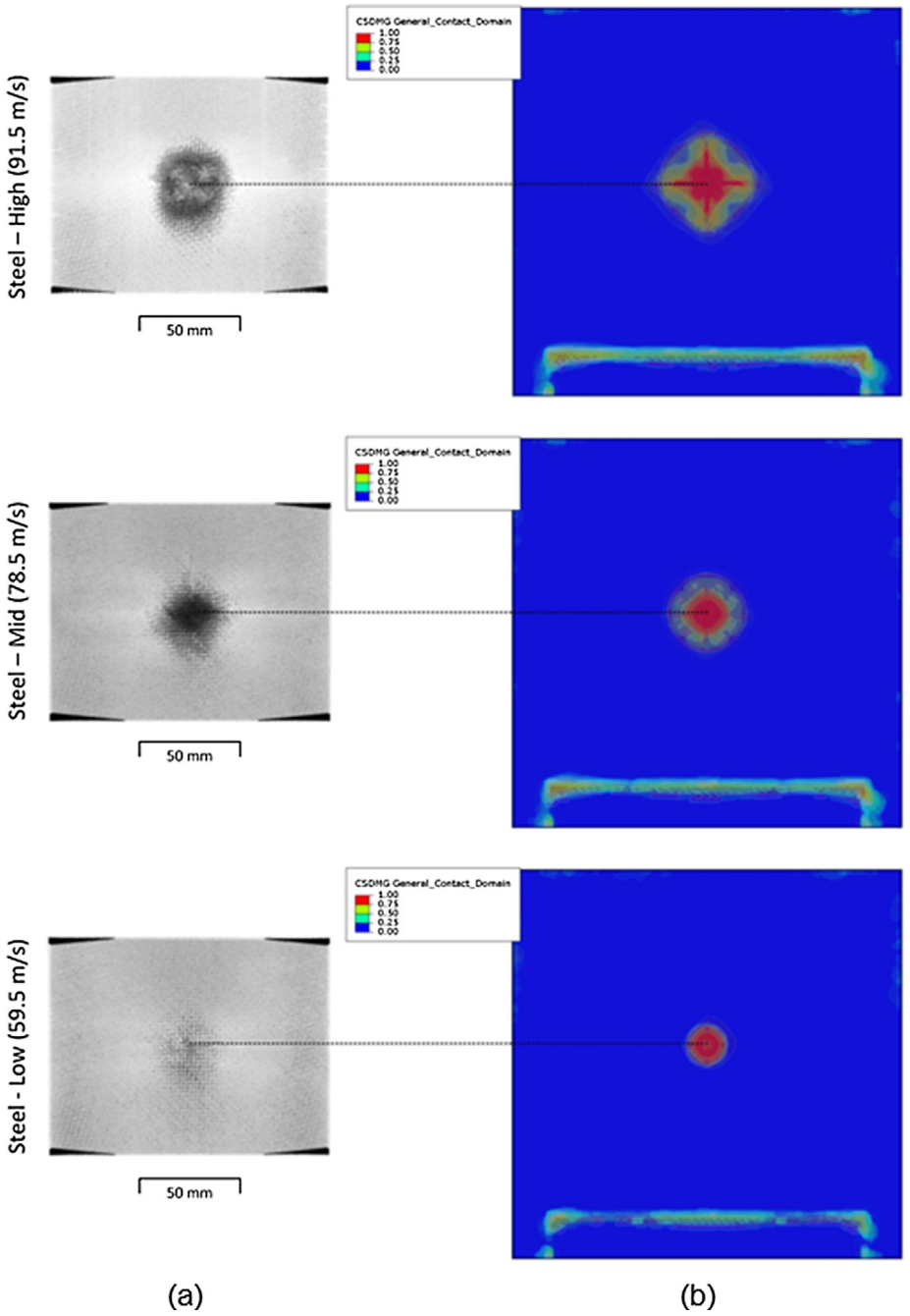

Fig. 11. Through-thickness damage cloud caused by ballistic steel impacts with different velocities: (a) micro CT; (b) FE simulations.

specimen's curvature during the loading process.

4.2. Damage analysis

The level of damage incurred in the composite due to impact was also analysed in the numerical simulations in comparison with the experimental data.

The major damage mode in steel-projectile impacts for an impact speed of 91.5 m/s was observed to be tensile fibre failure towards the rear of the sample (Fig. 10a) with very limited matrix damage localised at the point of impact (Fig. 10b). The through-thickness direction revealed the formation of a distributed cone of damage from the front to the back surface, typical for this type of impact. As expected for the rigid projectile, the damaged area remained highly localised for all loading conditions, with the matrix

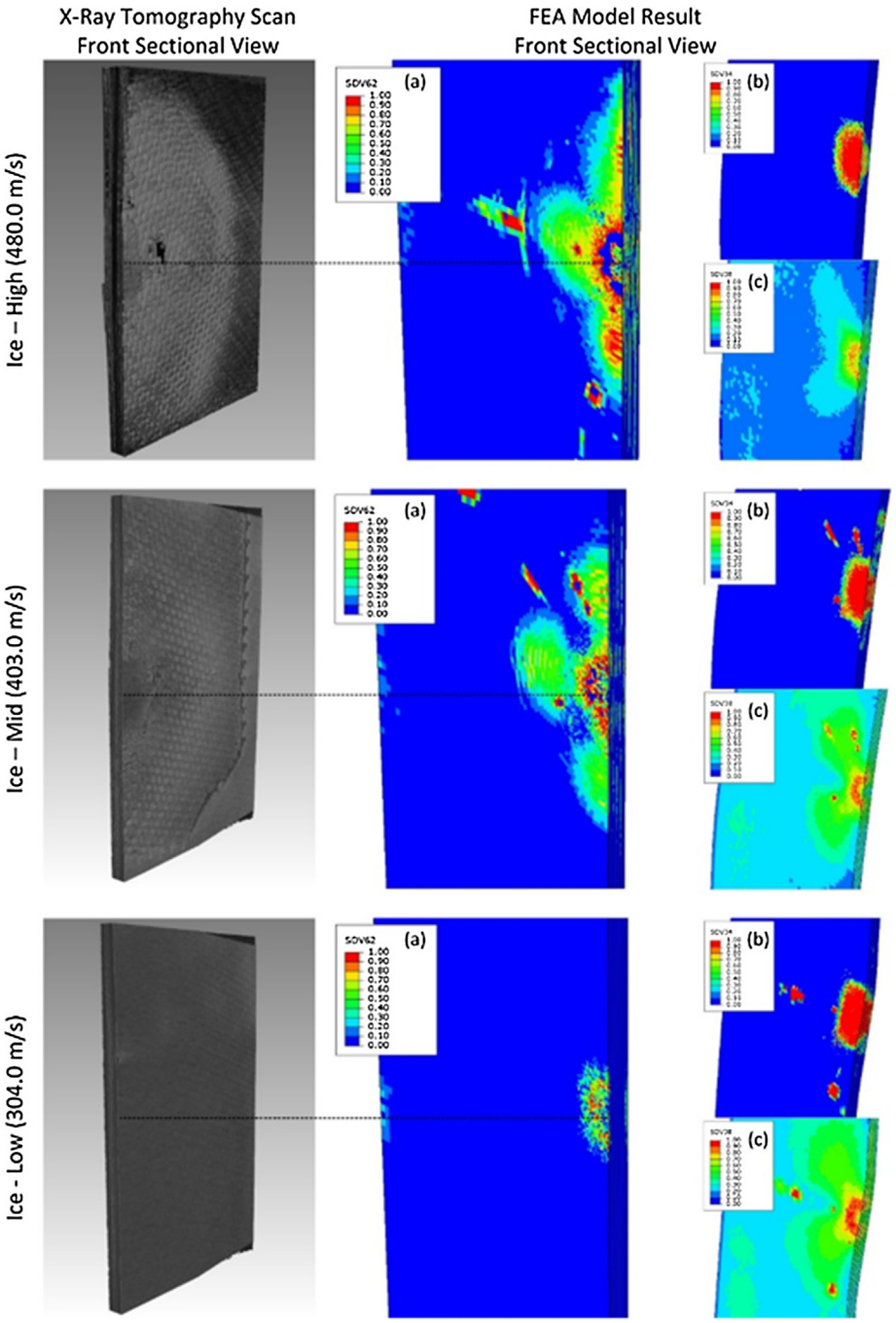

Fig. 12. Ballistic damage in ice-projectile impacts with different velocities: (a) fibre damage; (b) matrix damage; (c) shear damage.

(Fig. 10b) and shear damage (Fig. 10c) being almost identical. The fibre-failure area increased with the impact velocity as also witnessed in the experimental damage analysis in Part I. Overall, the calculated character of damage distribution within the model matched that of the experiments.

Analysis of the through-thickness damage in the CFRP specimens caused by the rigid-projectile impact (Fig. 11) showed that although the damaged area increased with the impact velocity, the damage remained highly localised. The simulations also revealed delamination at the lower edge of the specimen due to its fixture, reflected in the respective boundary condition (Fig. 2).

This was followed by a computational assessment of damage due to the ice-projectile impacts. The impact at the lowest velocity (304.0 m/s) showed no significant fibre damage (Fig. 12a), with limited matrix (Fig. 12b) and shear (Fig. 12c) damage.

Impacts with the medium (403.0 m/s) and high (480 m/s) velocities demonstrated increased levels of overall damage, with

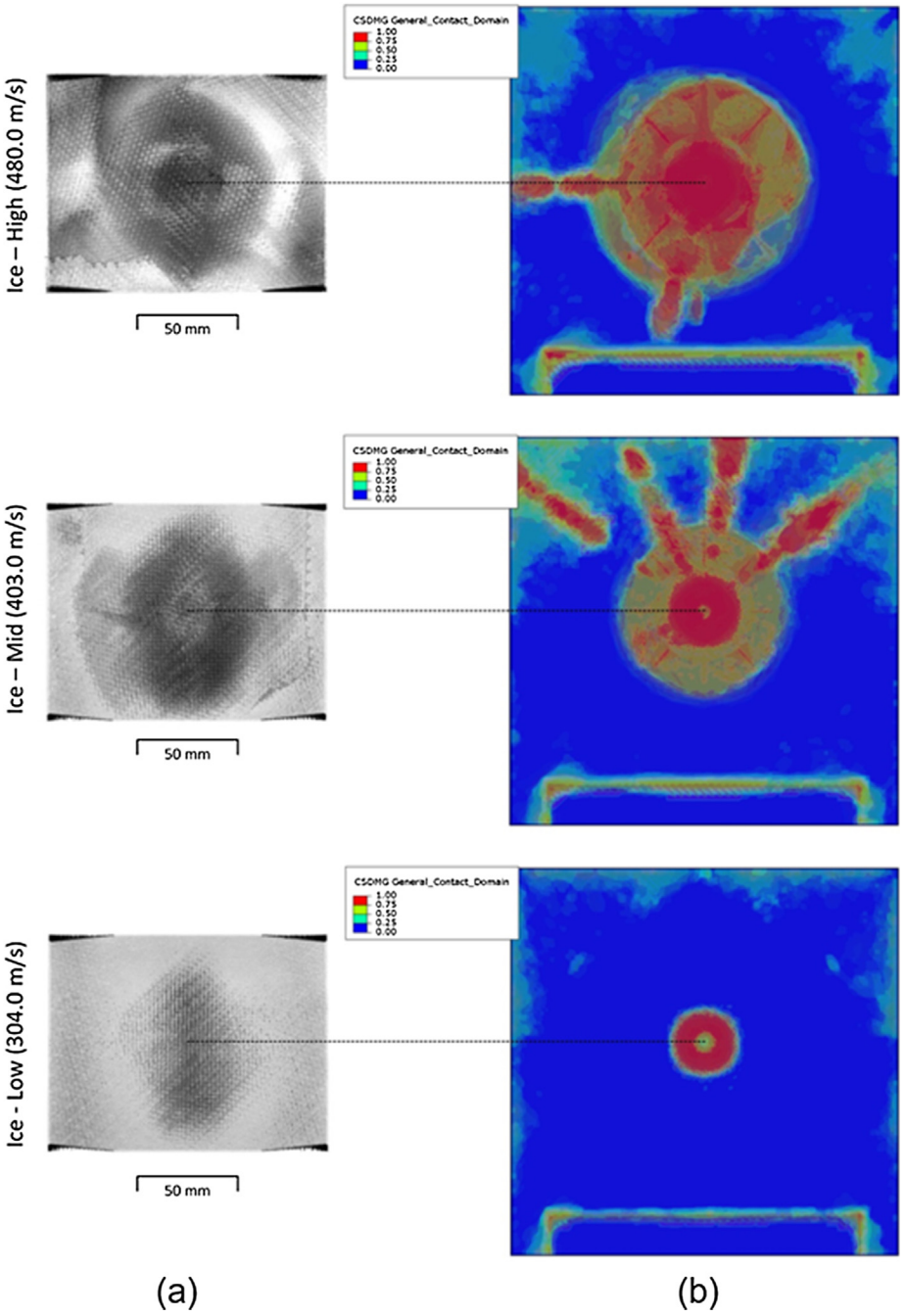

Fig. 13. Through-thickness damage cloud caused by ballistic ice impacts with different velocities: (a) micro CT; (b) FE simulations.

accurate reproduction of the main experimentally observed trends but with slightly reduced fibre failure at the front surfaces of the specimens resulting from the reduced indentation when compared to experiments. As a result, less damage was observed in the front-face plies as the projectile did not fragment inside the CFRP target. The primary reason for the discrepancy between the computational and experimental results was due to the complex deformation of ice projectiles, not fully adequately reproduced in the numerical simulations. It is possible that the tensile failure stresses were assumed to be too low resulting in premature fragmentation before the CFRP specimen could undergo the expected damage.

This damage enlarged with increasing projectile velocity and impact energy (Fig. 13), propagating considerably in CFRP specimens. The lower impact velocity (304.0 m/s) shows rather localised damage area (as observed in the experiment). At medium (403.0 m/s) and high (480 m/s) velocities, this area and the damage level increased significantly, matching the experimental trends.

Still, due to limitations of reproduction of the changing loading conditions during fragmentation of the ice projectile, numerical

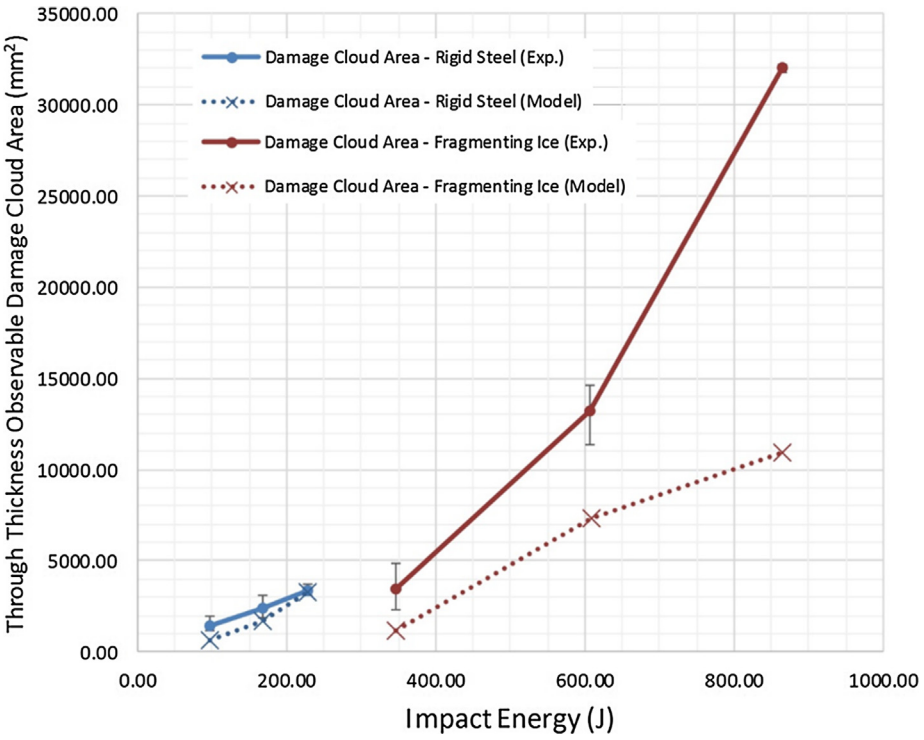

Fig. 14. Comparison of experimental and simulation results for damage areas at different impact energy for both types of projectiles.

simulations underestimated the extent of these processes. This is apparent in the quantitative data for the total damaged area presented in Fig. 14.

The calculated damage areas showed a good agreement with experiments for all loading regimes for the rigid-projectile impacts. For impacts with the ice projectiles, computational analysis of the minor damage generated results, closest to the experimental data. However, the numerical estimates deviated from experiments at higher velocities. Apparently, the increase in impact energy resulted in a much larger contact zone between the fragmented projectile and the specimen (Figs. 4–6). This research demonstrates that the model is suitable for more localised impact action; a process of delocalisation of impact energy as a result of ice fragmentation needs additional investigation.

Still, the results obtained with the VUMAT developed for the CFRP specimen is still deemed to be accurate to model deformation behaviour and damage evolution under various ballistic loading conditions, as far as the latter can be properly described.

5. Conclusions

In Part II, the ballistic response of the studied 2 × 2 twill woven CFRP composite was analysed using the suggested numerical approach based on a phenomenological continuum damage model. The developed material description was implemented in the ABAQUS Explicit FE software, used to simulate the evolution of deformation and damage in CFRP specimens in impacts with the rigid and fragmenting projectiles. For the former projectiles, the developed model showed a good agreement with the experimental data (Part I) for both the deformed horizontal and vertical profiles of the specimens and the underlying damage incurred. Clearly, the spatiotemporal development of out-of-plane deformations was a result of the interaction of a global dynamic response of the plate and the transient local contact (followed by indentation and penetration of the projectile). These processes were affected significantly by damage initiation and evolution, which, on the one hand, reduced the specimen's stiffness, thus changing the global deformation mode, and, on the other hand, interacted with local processes in the target beneath the contact area.

A transition to the fragmenting projectile introduced an additional level of complexity: a significantly changing contact area affected both the global deformation and damage localisation under this contact zone. The focus for further development of the numerical schemes for ice impacts should be on energy transfer in the processes of fragmentation and interaction of fragments with the CFRP target. An indentation and percolation of a few front-face plies at high velocities, followed by the transversal spread of fragments along the inter-ply interfaces and peeling-off of these plies, observed in the experiments (Part I), were not realised by the model. Instead, the process of ice fragmentation happened just on the target's surface.

This, by any means, is not a deficiency of the developed material's description, as validated by analysis of various impact cases for simpler loading conditions imposed by a rigid projectile. Hence, with a proper assessment (or simulation) of transient loading conditions, the developed approach can be used to analyse a response of woven CFRP composites to a broad range of dynamic events.

References

[1] Appleby-Thomas GJ, Hazell PJ, Dahini G. On the response of two commercially-important CFRP structures to multiple ice impacts. Compos Struct 2011;93:2619–27. https://doi.org/10.1016/j.compstruct.2011.04.029.

[2] Higuchi R, Okabe T, Yoshimura A, Tay TE. Progressive failure under high-velocity impact on composite laminates: experiment and phenomenological meso-modeling. Eng Fract Mech 2017;178:346–61. https://doi.org/10.1016/J.ENGFRACMECH.2017.03.019.

[3] Ullah H, Harland AR, Silberschmidt VV. Damage modelling in woven-fabric CFRP laminates under large-deflection bending. Comput Mater Sci 2012;64:130–5. https://doi.org/10.1016/J.COMMATSCI.2012.05.036.

[4] Zhang C, Duodu EA, Gu J. Finite element modeling of damage development in cross-ply composite laminates subjected to low velocity impact. Compos Struct 2017;173:219–27. https://doi.org/10.1016/J.COMPSTRUCT.2017.04.017.

[5] Lopes CS, Camanho PP, Gürdal Z, Maimí P, González EV. Low-velocity impact damage on dispersed stacking sequence laminates. Part II: Numerical simulations. Compos Sci Technol 2009;69:937–47. https://doi.org/10.1016/J.COMPSCITECH.2009.02.015.

[6] Phadnis VA, Makhdum F, Roy A, Silberschmidt VV. Drilling in carbon/epoxy composites: experimental investigations and finite element implementation. Compos Part A Appl Sci Manuf 2013;47:41–51. https://doi.org/10.1016/J.COMPOSITESA.2012.11.020.

[7] Shi Y, Swait T, Soutis C. Modelling damage evolution in composite laminates subjected to low velocity impact. Compos Struct 2012;94:2902–13. https://doi.org/10.1016/J.COMPSTRUCT.2012.03.039.

[8] Kachanov. Time of the rupture process under creep conditions. Izv Akad Nauk SSR Otd Tech Nauk 1958;8.

[9] Talreja R, Yalvac S, Yats LD, Wetters DG. Transverse cracking and stiffness reduction in cross ply laminates of different matrix toughness. J Compos Mater 1992;26:1644–63. https://doi.org/10.1177/002199839202601105.

[10] Talreja R. A continuum mechanics characterization of damage in composite materials. Proc R Soc A Math Phys Eng Sci 1985;399:195–216. https://doi.org/10.1098/rspa.1985.0055.

[11] Matzenmiller A, Lubliner J, Taylor RL. A constitutive model for anisotropic damage in fiber-composites. Mech Mater 1995;20:125–52. https://doi.org/10.1016/0167-6636(94)00053-0.

[12] Muñoz R, Martínez-Hergueta F, Gálvez F, González C, Llorca J. Ballistic performance of hybrid 3D woven composites: experiments and simulations. Compos Struct 2015;127:141–51. https://doi.org/10.1016/J.COMPSTRUCT.2015.03.021.

[13] Pernas-Sánchez J, Pedroche DA, Varas D, López-Puente J, Zaera R. Numerical modeling of ice behavior under high velocity impacts. Int J Solids Struct 2012;49:1919–27. https://doi.org/10.1016/J.IJSOLSTR.2012.03.038.

[14] Tippmann JD, Kim H, Rhymer JD. Experimentally validated strain rate dependent material model for spherical ice impact simulation. Int J Impact Eng 2013;57:43–54. https://doi.org/10.1016/J.IJIMPENG.2013.01.013.

[15] Hashin Z. Failure criteria for unidirectional fiber composites. J Appl Mech 1980;47:329. https://doi.org/10.1115/1.3153664.

[16] Puck A, Schürmann H. Failure analysis of FRP laminates by means of physically based phenomenological models. Compos Sci Technol 2002;62:1633–62. https://doi.org/10.1016/S0266-3538(01)00208-1.

[17] Berbinau P, Soutis C, Goutas P, Curtis PT. Effect of off-axis ply orientation on 0°-fibre microbuckling. Compos Part A Appl Sci Manuf 1999;30:1197–207. https://doi.org/10.1016/S1359-835X(99)00026-3.

[18] Berbinau P, Soutis C, Guz IA. Compressive failure of 0° unidirectional carbon-fibre-reinforced plastic (CFRP) laminates by fibre microbuckling. Compos Sci Technol 1999;59:1451–5. https://doi.org/10.1016/S0266-3538(98)00181-X.

[19] Koerber H, Xavier J, Camanho PP. High strain rate characterisation of unidirectional carbon-epoxy IM7-8552 in transverse compression and in-plane shear using digital image correlation. Mech Mater 2010;42:1004–19. doi: 10.1016/J.MECHMAT.2010.09.003.

[20] Daniel IM, Werner BT, Fenner JS. Strain-rate-dependent failure criteria for composites. Compos Sci Technol 2011;71:357–64. https://doi.org/10.1016/J.COMPSCITECH.2010.11.028.

[21] Hsiao HM, Daniel IM, Cordes RD. Strain rate effects on the transverse compressive and shear behavior of unidirectional composites. J Compos Mater 1999;33:1620–42. https://doi.org/10.1177/002199839903301703.

[22] Turon A, Dávila CG, Camanho PP, Costa J. An engineering solution for mesh size effects in the simulation of delamination using cohesive zone models. Eng Fract Mech 2007;74:1665–82. https://doi.org/10.1016/J.ENGFRACMECH.2006.08.025.

[23] Mendes PAAE, Donadon MV. Numerical prediction of compression after impact behavior of woven composite laminates. Compos Struct 2014;113:476–91. https://doi.org/10.1016/J.COMPSTRUCT.2014.03.051.

[24] Hosur M, Alexander J, Vaidya U, Jeelani S. High strain rate compression response of carbon/epoxy laminate composites. Compos Struct 2001;52:405–17. https://doi.org/10.1016/S0263-8223(01)00031-9.

[25] Melin GL, Asp EL. Effects of strain rate on transverse tension properties of a carbon/epoxy composite: studied by moiré photography. Compos Part A Appl Sci Manuf 1999;30:305–16. https://doi.org/10.1016/S1359-835X(98)00123-7.

[26] Hou J, Ruiz C. Measurement of the properties of woven CFRP T300/914 at different strain rates. Compos Sci Technol 2000;60:2829–34. https://doi.org/10.1016/S0266-3538(00)00151-2.

[27] Zhou G, Lloyd J, McGuirk J. Experimental evaluation of geometric factors affecting damage mechanisms in carbon/epoxy plates. Compos Part A Appl Sci Manuf 2001;32:71–84. https://doi.org/10.1016/S1359-835X(00)00119-6.

[28] Cruz J Il, Shah CH, Postyn AS. Properties of two carbon composite materials using LTM25 epoxy resin; 1996.

[29] Foroutan R, Nemes J, Ghiasi H, Hubert P. Experimental investigation of high strain-rate behaviour of fabric composites. Compos Struct 2013;106:264–9. https://doi.org/10.1016/J.COMPSTRUCT.2013.06.014.

[30] Hadavinia H, Ghasemnejad H. Effects of Mode-I and Mode-II interlaminar fracture toughness on the energy absorption of CFRP twill/weave composite box sections. Compos Struct 2009;89:303–14. https://doi.org/10.1016/J.COMPSTRUCT.2008.08.004.

[31] Ullah H, Harland AR, Lucas T, Price D, Silberschmidt VV. Finite-element modelling of bending of CFRP laminates: multiple delaminations. Comput Mater Sci 2012;52:147–56. https://doi.org/10.1016/J.COMMATSCI.2011.02.005.